


RESEARCH ARTICLE

A parametric model of the brain vascular system for estimation of the arterial input function (AIF) at the tissue level

Siamak P. Nejad-Davarani^{1,2,3}  | Hassan Bagher-Ebadian^{1,4} | James R. Ewing^{3,4} | Douglas C. Noll² | Tom Mikkelsen⁵ | Michael Chopp^{3,4} | Quan Jiang^{3,4}¹Department of Radiation Oncology, Henry Ford Health System, Detroit, Michigan, USA²Department of Biomedical Engineering, University of Michigan, Ann Arbor, Michigan, USA³Department of Neurology, Henry Ford Health System, Detroit, Michigan, USA⁴Department of Physics, Oakland University, Rochester, Michigan, USA⁵Department of Neurosurgery, Henry Ford Hospital, Detroit, Michigan, USA**Correspondence**Siamak P. Nejad-Davarani, Department of Radiation Oncology Henry Ford Health System Detroit, MI, 48202, USA.
Email: siamak@umich.edu**Funding information**

National Institutes of Health, Grant/Award Number: RO1NS64134

In this paper, we introduce a novel model of the brain vascular system, which is developed based on laws of fluid dynamics and vascular morphology. This model is used to address dispersion and delay of the arterial input function (AIF) at different levels of the vascular structure and to estimate the local AIF in DCE images. We developed a method based on the simplex algorithm and Akaike information criterion to estimate the likelihood of the contrast agent concentration signal sampled in DCE images belonging to different layers of the vascular tree or being a combination of different signal levels from different nodes of this structure. To evaluate this method, we tested the method on simulated local AIF signals at different levels of this structure. Even down to a signal to noise ratio of 5.5 our method was able to accurately detect the branching level of the simulated signals. When two signals with the same power level were combined, our method was able to separate the base signals of the composite AIF at the 50% threshold. We applied this method to dynamic contrast enhanced computed tomography (DCE-CT) data, and using the parameters estimated by our method we created an arrival time map of the brain. Our model corrected AIF can be used for solving the pharmacokinetic equations for more accurate estimation of vascular permeability parameters in DCE imaging studies.

KEYWORDS

arterial input function, dynamic contrast enhanced imaging, laminar flow, perfusion, vascular modeling, vascular permeability

1 | INTRODUCTION

Estimating the arterial input function (AIF) of a contrast agent (CA), the time-concentration curve in plasma, especially at the tissue level, has long presented a challenge in dynamic contrast enhanced magnetic resonance (DCE-MR), dynamic contrast enhanced computed tomography (DCE-CT) and dynamic susceptibility contrast (DSC) imaging studies. The AIF is used for estimating mean transit time (MTT), cerebral blood flow (CBF), cerebral blood volume (CBV), vascular transfer rate constant (K^{trans}), vascular plasma volume (v_p), and extracellular-extravascular space (v_e) in DSC and DCE studies.^{1,2} Using an inaccurate

AIF profile in permeability and perfusion analyses could substantially add bias to the estimated hemodynamic and permeability maps. This is one of the main reasons for finding the AIF at the tissue level or in other words, the local AIF. One of the approaches to solving this problem is modeling the vascular system in the brain and using this model to find the dynamics of blood flow at the capillary (tissue) level.

Many researchers have attempted to model vasculature for applications in DSC and DCE studies. Depending on the applications, there have been different approaches to this problem, each having their advantages and shortcomings. One approach has been modeling the blood circulatory system of the whole body and finding the flow at different locations in the vascular system. In this category, Sherwin et al. built a one-dimensional network based on space-time variables and linear and non-linear modeling.³ Another modeling approach is based on having a three-dimensional arterial tree embedded in a one-dimensional representation of the arterial system.⁴ Bagher-Ebadian et al. suggested a model and algorithm based on the blood-circulatory system, to estimate the CA time-concentration

Abbreviations: ACA, anterior cerebral artery; AIC, Akaike information criterion; AIF, arterial input function; ASL, arterial spin labeling; CA, contrast agent; CBF, cerebral blood flow; DCE-CT, dynamic contrast enhanced computed tomography; DCE-MR, dynamic contrast enhanced magnetic resonance; DSC, dynamic susceptibility contrast; K^{trans} , vascular transfer rate constant; MCA, middle cerebral artery; MTT, mean transit time; PCA, posterior cerebral artery; RSS, residual sum of squares; SNR, signal to noise ratio; v_e , extracellular-extravascular volume; v_p , vascular plasma volume

curve in arterial plasma after an intravenous bolus injection.^{5,6} Although the models above allow us to perform quantitative and qualitative studies of local and global hemodynamic quantities, none of these models have addressed the model of blood flow at the capillary (tissue) level in the brain.

In one study Calamante et al. proposed using independent component analysis (ICA) in perfusion studies as a tool to define a local AIF to obtain more accurate quantification of CBF in DSC-MRI studies.⁷ The method for finding the local AIF was based on a semi-manual approach and user input was required for choosing the components; moreover, there was no method for validating the local AIF. Mouridsen et al. defined a physiological estimation of microvasculature, which was used for estimation of cerebral perfusion with Bayesian methods.⁸ In this study, it was assumed that the AIF has a gamma variate probability density function. Assuming gamma variate or exponential decay functions for the local AIF have been used in other studies as well.^{9,10} Cebra et al. used a method based on MR angiograms to develop detailed assessment of blood flow patterns from direct *in vivo* measurements of vessel anatomy and flow rates using finite element methods.¹¹ The focus of this research was only on major arteries and small arteries were not modeled.

There have been a considerable number of studies for modeling changes in the AIF for arterial spin labeling (ASL) applications. Some have used Gaussian kernels¹² or variations of these¹³ for modeling dispersion of the AIF, which provide plausible smoothing of the AIF box-car shape along the arterial pathway. Hernandez-Garcia et al. previously presented a one-dimensional model for ASL applications that takes into account the effects of transit times by modeling displacement and decay of the inversion tag between the tagging and imaging locations.¹⁴ In another study, Kazan et al. modeled the effects of dispersion in ASL¹⁵ using the mass transport equation. In another study Gallichan and Jezzard modeled dispersion of the AIF using laminar (parabolic) and pulsatile flow of blood in major arteries.¹⁶ This model was designed only for ASL applications and also it considered only a single tube with no branching, which is not the case in vascular structures. Later, Chappell et al. used a variation of this model with a gamma-variate kernel added to address dispersion in ASL.¹⁷ Although these studies have suggested practical approaches for addressing changes of the ASL bolus, none of them have considered the effects of multiple pathways of flow through the vasculature for modeling the overall dispersion. One of the approaches that has used laws of fluid dynamics to estimate the changes in the bolus profile is a method proposed by Gall et al.¹⁸ They introduced a framework for solving the deconvolution problem in DSC using a functional form of the residue function and also for estimating the changes in the bolus profile in ASL applications. In this framework, the function was derived based on the laws of laminar flow and a vascular tree model. Their results of using this function showed excellent agreement with data measured using ASL in early branches of the vascular tree.

The methods discussed above show different models for the AIF, but most of these models either represent the input function only at the level of the major arteries (such as the carotid artery), or if they have an estimation of the input function at a lower level, the model does not represent all the major parameters that affect the AIF at the capillary level. Here, using an approach similar to the work done

by Gall et al.¹⁸ and Kellner et al.,¹⁹ we introduce an analytical model of dispersion in major arteries at different levels of branching based on laws of fluid dynamics and morphological properties of the vessels. Next, using this model and the Akaike information criterion (AIC), we introduce a method for estimating the structure of the vascular tree at different locations in DCE images.

2 | MATERIALS AND METHODS

2.1 | Implementation of the vasculature model

The model we have proposed explains dispersion of the AIF based on two different sources: dispersion in a single vessel due to laminar flow and dispersion due to branching of the vessels down to the capillaries and multiple arrival times of blood in the tissue due to different vascular pathways of different lengths. All modeling and visualization was done in MATLAB (Release 2010b, MathWorks, Natick, MA, USA).

2.1.1 | Parametric expression of dispersion in single tube

The average Reynolds number (Re) for the carotid artery has been calculated to be 266 and 911 for mean and peak flow rates respectively,²⁰ and since this is less than 4000 we consider the flow of blood in the brain vessels other than the capillaries to be laminar. In laminar flow, the velocity of the fluid in a tube is dependent on the radial distance to the center of the tube and can be characterized as²¹

$$v = v_0 \left(1 - \frac{r^2}{R^2} \right) \quad (1)$$

where v_0 is the velocity of blood along the central axis of the vessel with a radius of R . v is the blood velocity at radial distance r from this axis. In this study, considering the time resolution of DCE imaging, the effects of pulsatile flow of blood in the vessels are ignored and it is assumed that flow has reached a steady state; thus, from this point on, v_0 will represent the maximum blood velocity in each vessel. Based on Equation 1, in an approach similar to the work by Gall et al.²² and Kellner et al.,¹⁹ we have derived a transfer function that describes the distortion of the CA profile, after passing through a single vessel (details are presented in the appendix):

$$h(t) = \begin{cases} 0 & t < t_0 \\ \frac{2t_0^2}{t^3} & t \geq t_0 \end{cases} \quad (2)$$

where

$$t_0 = \frac{D_0}{v_0} \quad (3)$$

D_0 is the length of the vessel, and since v_0 is the maximum velocity of blood in the vessel, t_0 is the shortest time that the CA takes to pass through the vessel; under the assumption of steady flow in the vascular system t_0 can be considered a characteristic of the vessel.

2.1.2 | Dispersion due to the cascade of vessels

In the case where a cascade of vessels exists, the overall transfer function of the vessels from the input node to any node in the system is the convolution of the transfer functions of the individual vessels in the

pathway. In such a system, the transfer function of each vessel can be written as follows:

$$h(t)_1 = \frac{2t_{01}^2}{t^3} \quad \text{for } t \geq t_{01} \quad (4)$$

$$h(t)_2 = \frac{2t_{02}^2}{t^3} \quad \text{for } t \geq t_{02} \quad (5)$$

$$h(t)_3 = \frac{2t_{03}^2}{t^3} \quad \text{for } t \geq t_{03} \quad (6)$$

$$h(t)_n = \frac{2t_{0n}^2}{t^3} \quad \text{for } t \geq t_{0n}. \quad (7)$$

In these functions, t_{01} to t_{0n} are the time delays of each individual vessel along the vascular route, from the opening of the main artery down to the n th branching layer. The transfer function of the vessels from the main input to the n th level of sub-branches can be written as

$$h(t)_{1 \text{ to } n} = h(t)_1 * h(t)_2 * \dots * h(t)_n. \quad (8)$$

2.1.3 | Fractal geometry of the vessels

Based on Murray's branching law of vessels, when an artery bifurcates, the radii of the daughter vessels are related to the radius of the parent vessel through^{23,24}

$$r_p^3 = r_{d1}^3 + r_{d2}^3 \quad (9)$$

If we assume that the two daughter branches are similar, the radii of these daughter vessels and the parent vessel will be related through

$$r_d = \frac{r_p}{\sqrt[3]{2}} \quad (10)$$

Therefore, the maximum velocity of blood in each of the daughter vessels (v_{0d}) will be $\sqrt[3]{2}$ times that of the parent vessel (v_{0p}). Also if we assume that the length of the daughter branches is

$$l_d = \frac{l_p}{\sqrt[3]{2}} \quad (11)$$

the delay time of the daughter vessels (t_{0d}) will be equal to the delay time of the parent vessel (t_{0p}). The benefit of employing these assumptions is that, while they are close to reality,²⁵ it can reduce the number of parameters that describe a vascular tree; instead of having an individual t_0 for each branch, one t_0 can describe the entire tree from the major artery down to the arterioles. In this case, if $h(t)_1$ is the transfer function of each branch, the general equation for the transfer function of the vascular tree will be

$$h(t)_{1 \text{ to } n} = [h(t)_1]^{*n} \quad (12)$$

where “* n ” denotes n repeated convolutions.

2.1.4 | Simulating the CA concentration profile at different levels of the vascular structure

To explore the feasibility of using our method for estimating the vascular transfer function parameters in DCE images, we first performed a simulation of the CA concentration profiles. Initially we implemented a vascular morphological model as in Figure 1, with parameters comparable to real life values. The diameter of the common carotid artery in healthy adults has been estimated to be²⁶ 6.0 ± 0.8 mm and the mean velocity of blood passing through the internal carotid artery has been measured to be 32.7 ± 3.0 cm/s in healthy adults.²⁶ These values were used as the starting points of our model implementation. Based on the findings of Wright et al.,²⁸ the mean and standard deviation of the branch lengths in the brain is 25.02 ± 2.71 mm (19.35 mm–30.14 mm). The length of the main branch of our model was set to 4 cm based on these reported values. The model starts with one main artery; this artery bifurcates and two daughter vessels are created with the length and radius described in the previous section.

Using the same procedure, the daughter branches can be created recursively till they reach the capillary level. The three main arterial branches originating from the circle of Willis are the anterior cerebral artery (ACA), middle cerebral artery (MCA) and posterior cerebral artery (PCA).²⁷ Each of these major vascular trees feeds a different part of the brain, but since they all originate from the circle of Willis, considering the relatively low time resolution of the imaging modalities, we assumed that the CA concentration profiles of the blood entering these three branches are similar. According to the measurements made by Wright et al.,²⁸ the maximum numbers of bifurcations in these trees are 6.15 ± 1.53 (ACA), 8.80 ± 1.40 (MCA), and 5.93 ± 1.66 (PCA). Using these initial values and branching rules, our model was implemented

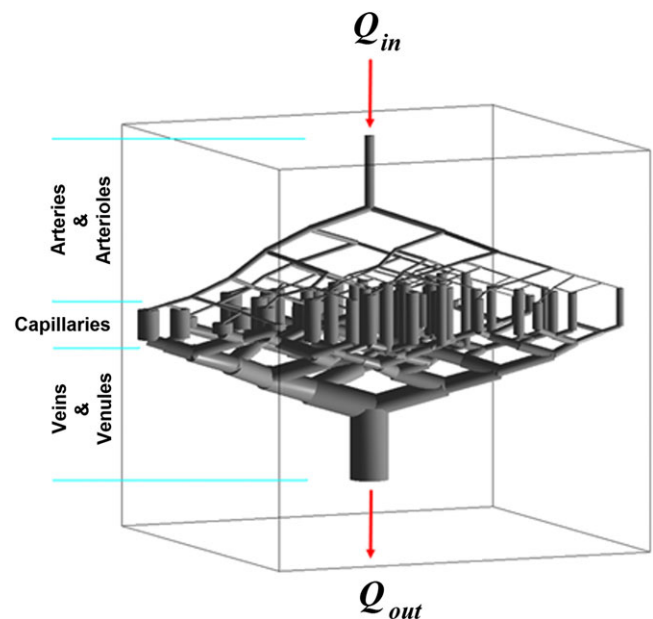


FIGURE 1 Morphological structure of the vascular model; branching of arteries and arterioles has been simulated down to six levels. As seen here, the veins and venules have larger volume and diameter compared with arteries and arterioles. The volumetric flow rate of blood entering this model is equal to the efferent flow. Every segment of the capillary bed is modeled as a single tube vessel in which the flow is non-laminar

with six levels of branching down to the capillary level as in Figure 1; the veins and venules were implemented as the mirror image of the arteries and arterioles, albeit with a larger radius such that the overall volume of the veins and venules was four times that of the arteries and arterioles.²¹

The flow rate in the vessels in this model was calculated by finding the resistance of every branch based on Poiseuille's law²¹ and converting the model to an analogous electric circuit and finding the electric current in all branches based on Ohm's law.²⁹ After finding the velocity of blood in all branches of the model, the time delay (t_0) of each branch was calculated using Equation 3 and the vascular transfer function between the opening of the main artery and every node was estimated based on Equation 12. Figure 2A shows the transfer functions between the opening of the main artery and the end of each of the vessels in the vascular structure, down to the sixth layer of

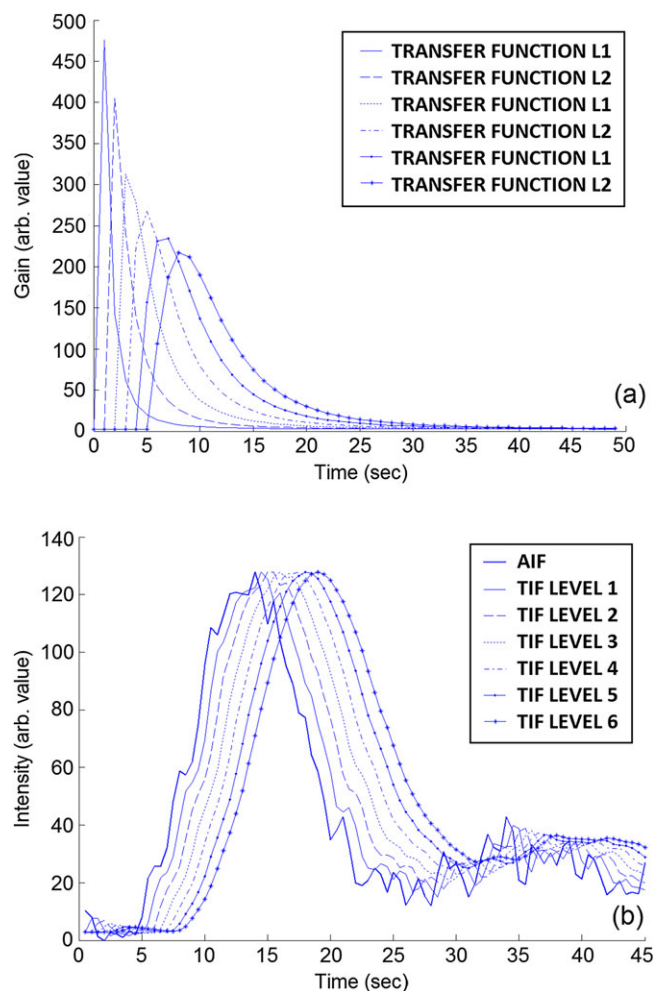


FIGURE 2 A, The transfer functions of vessels from the opening of the main artery down to the sixth level of the vascular branching. As seen here, as the level increases, the arrival time and dispersion both increase. B, Plots of the main AIF (bold curve) of a human subject along with the local AIFs at six levels of our vascular model estimated by convolving the main AIF with the transfer function at each level. The AIF was sampled from the first 45 s of the DCE-CT image series in the voxels showing the internal carotid artery of a human subject after the bolus injection of the CA. For easier comparison of the profile of these curves, the peaks are scaled to the peak of the AIF. As seen here, by moving to the higher levels of the vascular structure, the arrival time delay becomes longer and the curves become more dispersed

branching in one vascular line. Using the profile of the CA in the carotid artery of a human subject in a DCE-CT image series (acquired by the procedure that will be described in the following sections) and these six transfer functions, the local AIF at every node was calculated, as plotted in Figure 2B. For better visual comparison of these curves, the peaks are all scaled to the same level as the AIF. By moving to higher levels of the vascular tree, the arrival time of the CA profile increases and it also becomes more dispersed.

2.2 | Estimating the vascular level of a DCE signal

In this section we describe the method we have used for solving the inverse problem which is estimating the values of the time delay (t_0) of the vascular tree based on the CA profile sampled in the brain tissue; this can be used for both the simulated data and data from DCE images.

2.2.1 | Fitting the data to the models

Every voxel in the image volume belongs to one part of the vascular tree or the capillary bed; however, except for a few major vessels, it is not visually possible to follow the level of vessels in the branch hierarchy. The goal is to determine the likelihood of each voxel belonging to different branching levels of the vascular tree structure. The first step is to estimate a transfer function (according to Equation 12) that when convolved with a global AIF can result in the CA concentration profile of that voxel. For practical purposes, to compensate for the signal reduction due to volumetric fraction of vessels in tissue, a gain factor g was added to the transfer function:

$$h(t)_{1 \text{ to } n} = g \times [h(t)_1]^{*n} \quad (13)$$

The global AIF profile is defined as $AIF(t)$ and the measured tissue concentration signal of an arbitrary voxel in the brain image as $CA(t)$. The relationship between these two can be defined as

$$CA(t) = AIF(t) * h(t)_{1 \text{ to } x} \quad (14)$$

where x is the branching level of the vessels in this voxel, which generally speaking is initially an unknown value, and one of the goals is to determine the possible value (or values) of x for this voxel. It should be noted that in this equation the effects of the capillary bed on dispersing the AIF have been neglected. Using the simplex algorithm³⁰ as a non-linear fitting method and the sum of squared errors as the cost function, for every possible configuration of the transfer function ($h(t)_{1 \text{ to } 2}$, $h(t)_{1 \text{ to } 3}$, ... or $h(t)_{1 \text{ to } 6}$), the best function transforming the reference $AIF(t)$ to $CA(t)$ is found. This results in six different configurations of the transfer function where each is described by $[g, t_0, n]$, where n varies from 1 to 6 and represents the branching level of the vessel. It should be noted that the parameters estimated for every configuration of the transfer function are not dependent on the parameters from other configurations and are estimated independently every time the fitting procedure is repeated.

2.2.2 | Model selection and model averaging using AIC

After finding the six best transfer functions (one for each of the six branching layer configurations) or the model configurations for every voxel, the problem of determining the contribution of each model configuration should be addressed. This is necessary since each voxel might be representing a combination of vessels from different layers of the vascular structure; or, if it is the representative of only one vessel or tissue type, the branching level of the vessel at this voxel needs to be estimated. In our study, we used the AIC for model selection and model averaging.³¹ The AIC value can be calculated using the residual sum of squares (RSS) for each of the six models being investigated using the following equation:

$$AIC = 2k + 2 \frac{k(k+1)}{n-k-1} + n \ln \left(\frac{RSS}{n} \right) \quad (15)$$

Here n is defined as the number of observations, which in our study represents the number of image time points. k is the number of model configuration parameters, which in our application is two for each model configuration. We define AIC_{min} as the AIC for the model configuration with the best fit. To calculate the Akaike weights, we first define a new variable Δ_i that represents the difference between the AIC values in these six model configurations with the lowest AIC value:

$$\Delta_i = AIC_i - AIC_{min} \quad \text{for } i = 1, 2, \dots, 6 \quad (16)$$

Using these values, the Akaike weight (w_i) for each model configuration is estimated:

$$w_i = \frac{\exp(-0.5 \Delta_i)}{\sum_{j=1}^6 \exp(-0.5 \Delta_j)} \quad (17)$$

For each voxel, the estimated Akaike weights are considered to be the probability of model configuration i ($i = 1$ to 6) being the best model to describe the transfer function between the opening of the main artery and this voxel. Using the Akaike weights and the estimated values of the model parameters for each configuration of the model an average transfer function is calculated, which we name $h(t)_{est}$. Using this transfer function, the local AIF can be estimated as follows:

$$AIF_L(t) = AIF(t) * h(t)_{est} \quad (18)$$

In our model, we have not included the effects of the capillaries on the AIF, and therefore the transfer function that is estimated using the method explained above will give an estimation of the transfer functions of the arteries and arterioles feeding the capillary bed, which is the reason why in this equation we have referred to it as $AIF_L(t)$.

2.2.3 | Delay maps

As explained before, every transfer function is described with a set of parameters $[g, t_0, n]$. In the case of dealing with only one model configuration, the total delay time from the main artery opening to the voxel being studied (or the arrival time of the CA) can be calculated as $n \times t_0$; however, in this study, since multiple model configurations are used, by applying the rules of model averaging using the AIC,³² the delay time (CA arrival time) of each voxel is estimated by calculating a weighted sum of the delay times of all model configurations, with the

weights being the Akaike weights of this voxel:

$$t_{Total} = \sum_{i=1}^6 w_i \times i t_{0i} \quad (19)$$

where t_{0i} is the t_0 of the model configuration with i branching levels. The benefit of using this model averaging method³² to calculate the delay time is that voxels representing tissues that are being supplied by more than one branching level of the vascular system will have all these vessels accounted for, and the delay time will be a weighted average of all the possible delay times from different vascular pathways. This approach can also address the concept of collateral flow. Previously, Brix et al. used a similar weighted model approach for finding the best approximating model from three nested compartmental pharmacokinetic model for analysis of tissue microcirculation.³³

2.3 | Model evaluation using DCE-CT imaging

The next step of vascular model development was evaluating the performance of the model using human DCE data. After studying different dynamic imaging modalities, DCE-CT imaging was selected as this modality. Compared with DCE-MRI, DCE-CT images have lower signal to noise ratio (SNR) and contrast to noise ratio.³⁴ However, other characteristics of this modality made it a better choice for our study: the signal intensity of the CT images is linearly dependent on the CA concentration,³⁵ and also the temporal resolution of this modality is much higher (~ 10 times) than DCE-MR images (0.5 s versus 5 s). In addition, CT images have better spatial resolution.³⁶

The study was approved by the Henry Ford Health System Institutional Review Board and written informed consent was obtained from the subject. DCE-CT images were acquired on a GE LightSpeed VCT scanner with image matrix size of 512×512 (24×24 cm² FOV) and eight slices (5 mm slice thickness) with 99 imagepacks (89 image sets sampled every 0.5 s for the first 44 s, one image acquired at the 50 s time point, followed by nine image sets acquired every 16 s for a total scan time of 194 s). 50 ml of iodinated CA with a concentration of 0.5 ml/kg was injected as a bolus using a power injector at a rate of 4 cc/s starting 5 s after start of image acquisition; the cine scan was done for 50 s. The dynamic images were baseline corrected to make their intensity linearly dependent on the CA concentration. Also, to increase the SNR, especially in the tissue regions, the neighboring voxels were averaged and the images downsized to 128×128 . After these pre-processing steps, the CT images were ready to be used for testing the model using the approach explained in the previous sections.

3 | RESULTS

3.1 | Simulation results

3.1.1 | Estimation of the level of the simulated CA concentration profiles

The goal of the first part of our simulation was to explore the ability of our method to find the correct transfer function of the vascular structure based on the AIF and the simulated CA concentration profiles as explained previously. The different model configurations were fit to

each of the six profiles using the fitting procedure and the model selection methods that we described. The likelihood of these profiles belonging to each of the different model configurations was estimated using the fitting residue value and the Akaike method. The effect of noise on the performance of the model was evaluated by adding

different levels of noise to the simulated profiles. Figure 3A shows the results of these simulations. As seen here, the added noise level is varied between 0% to 100%, and at each of these levels the likelihood of selecting the correct level of the vascular structures has been estimated. Up to the 18% noise level, the likelihood of selecting the

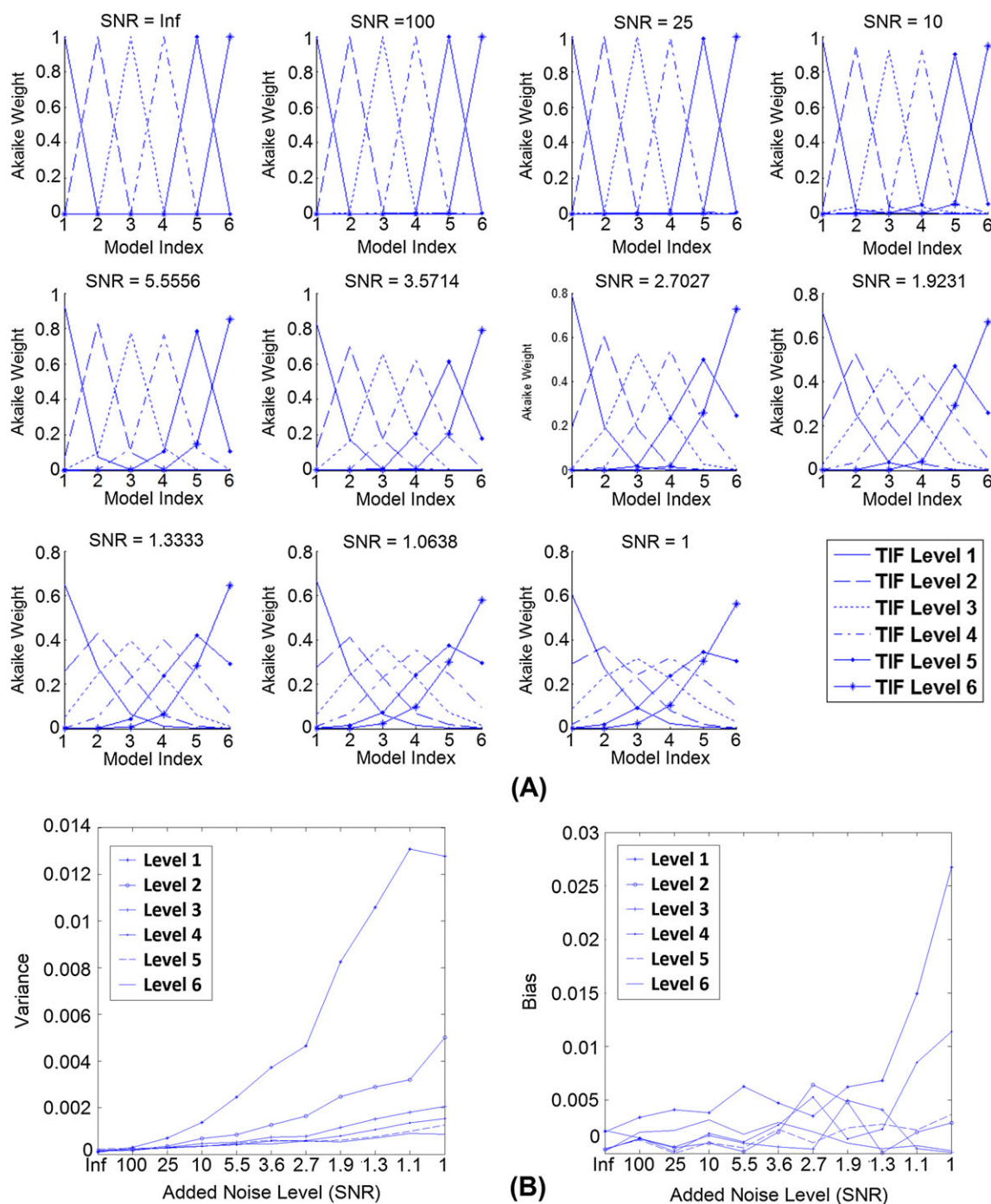


FIGURE 3 A, Akaike weights of each of the simulated signals after model averaging. The plots show the likelihood of each of the simulated local AIFs being selected as the level of branching that they were simulated for. As seen here, even at the 18% noise level, the likelihood of picking the correct branching level of the signal is almost unity for all cases. As the noise level increases, the accuracy of the system decreases and the likelihood of picking the correct model configuration decreases; however, at the 100% noise level, the likelihood of picking the correct level index does not go below 0.3. B, Bias and variance of the estimated parameters for the six configurations of the model for 11 levels of Gaussian noise added to the signal. These values are estimated with the described procedure and for 300 repetitions at each noise level. When the vascular structure has only one level, only one time delay is estimated and the curves represent the values of this parameter. For higher levels of vascular branching, the sum of the estimated parameters is used. As seen here, for all levels of noise, the estimates of these parameters remain very close to the original values of these parameters. One of the sources of bias can be the temporal resolution of the simulated signals

correct level of the profile is almost unity for all cases. As this noise level increases, the accuracy of the system decreases and this likelihood decreases; however, at the 100% noise level, the likelihood of selecting the correct level index does not fall below 0.3.

In Figure 3B, the bias and variance of the estimated parameters are plotted. These values are estimated with the procedure described above. In these graphs, each data point shows the bias and variance of the values for each noise level. As seen here, for all levels of noise, the estimates of these parameters remain very close to the original values of these parameters. One of the reasons for the bias in the estimated values can be the temporal resolution of the simulated data.

3.1.2 | Decomposing the simulated composite profile

When applying our method to the DCE-CT images, it is likely that the signal sampled from a typical voxel in the image represents a composite of vessel segments from more than one level of the vascular tree, which can also be the result of collateral flow in cranial vasculature. To simulate these conditions, and to explore the feasibility of our method for detecting these signals, the superposition of the CA profile from different levels of the model was created and decomposed by the fitting algorithm and by applying the AIC method as explained before.

Figure 4 shows a schematic diagram of our model simulation in the case when two signals are combined. Here, the square represents a hypothetical voxel in which vessels from both the second and sixth levels pass through. The temporal signal sampled in this voxel, is the weighted sum of the signals from the two vessel segments, and depending on the effective volume of each of them in this voxel, the level of contribution of each signal is adjusted from 0% to 100%. Also, we added different levels of noise to the composite signal (0% to

100%) and explored the feasibility of our method to decompose these signals in the presence of noise.

Figure 5 shows the curves representing the Akaike weights of the composite signals after decomposition by the method explained above. Each curve represents the average of decomposition results from 300 repetitions at each noise level. As seen here, at noise levels lower than 50%, almost all these curves meet at the 50% contribution level point, which matches our expectation. One observation in these curves is that in cases where the contribution of either signal is not close to 50%, when no noise is added to the signals or the noise level is small, the Akaike weights tend to become saturated to unity or zero; this is due to the large difference in the residue values of the fitting procedure for the two signals in the absence of noise. However, when noise is added, since the residues will have large values, the Akaike weights will not become saturated in these cases. When the difference between the levels of the two signals increases, this saturation effect will become more evident, even in the presence of noise. These results show that, in the no-noise situation, the AIC does not act as an unbiased estimator.

3.2 | Results of applying the model to DCE-CT images

Figure 6 shows the tissue concentration signals sampled from four different regions (circle of Willis, a small artery which was a sub-branch of the MCA, a region of the normal tissue and the superior sagittal sinus) and the corresponding tissue input signals estimated using Equation 18. These curves show that the proposed method can describe the transfer function for the arteries and capillaries very well and the reconstructed signal matches the tissue concentration signal sampled from

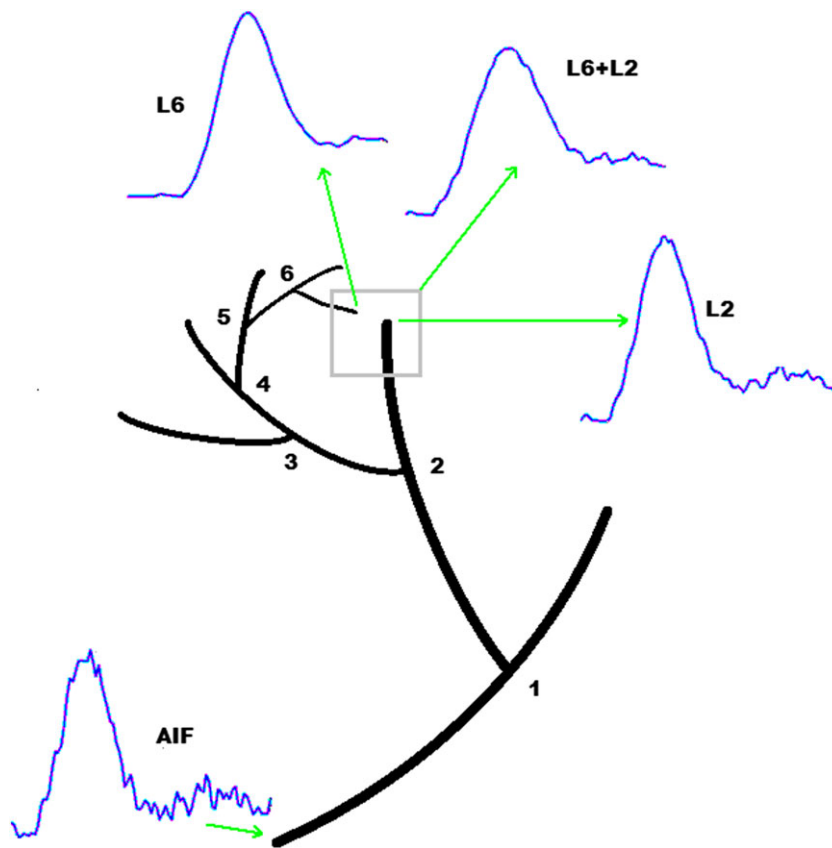


FIGURE 4 Schematic figure showing a typical AIF from one of the major cerebral arteries of a human subject in DCE-CT images and the simulated local AIFs at the second (L2) and sixth (L6) levels of our vascular model. In this figure the effect of one voxel representing vessels from two different levels has been simulated. In this case the signal sampled from this voxel would be the superposition of the two signals (L6 + L2). Using this configuration, we have studied the feasibility of our method to distinguish and separate the signals that form the composite signal

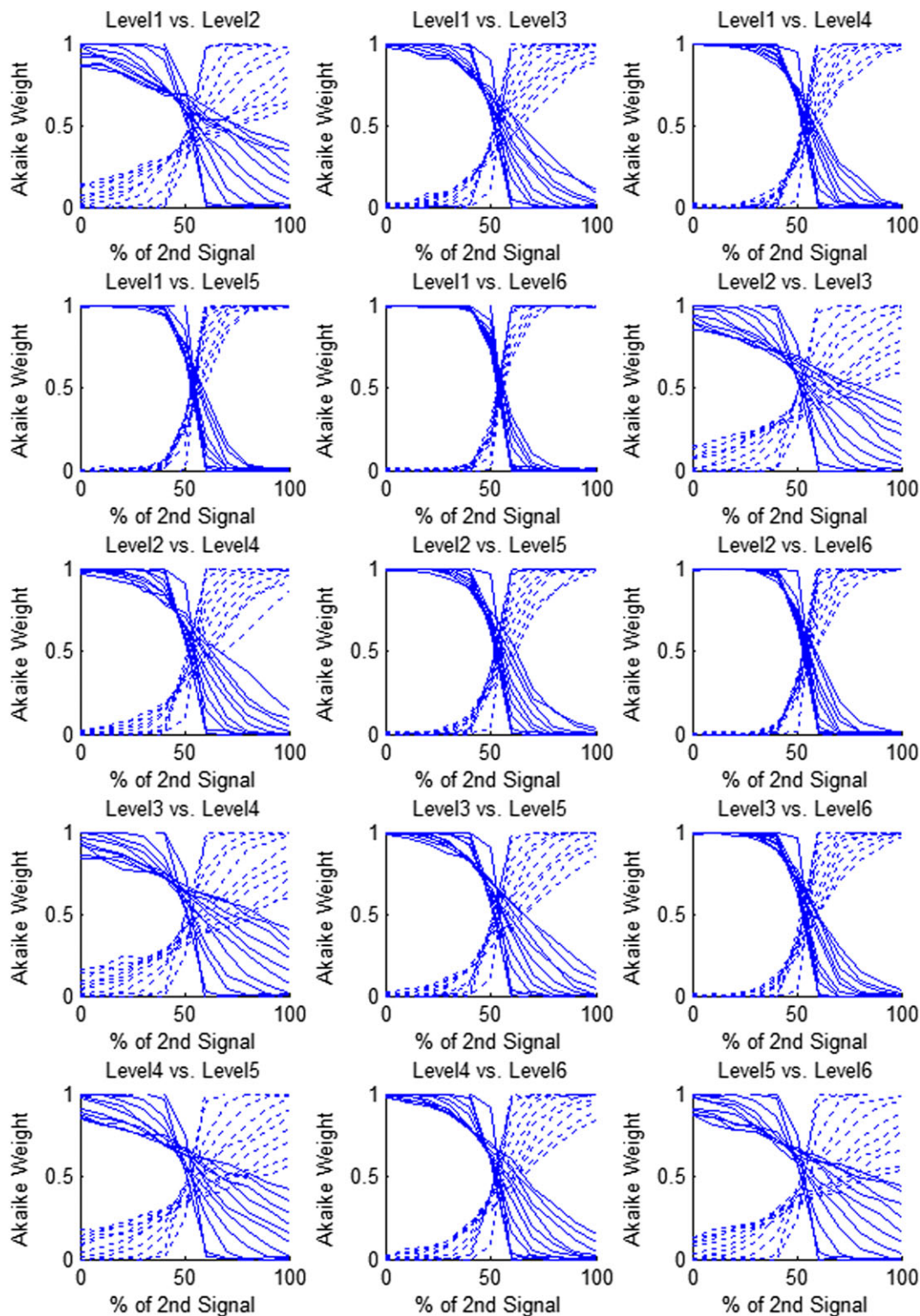


FIGURE 5 Akaike weights of the simulated composite signals after decomposition. Each curve represents the average of decomposition results of 300 repetitions at each noise level. The composite signal is basically the weighted sum of the two simulated signals (the x-axis represents the percentage of contribution of the second signal in the composite signal) from different layers of the vascular structure. In each of the boxes above, each plot represents one noise level: in the upper half of the box, from left to right, each dotted line indicates 0% to 100% noise level (SNR = infinity, 100, 25, 10, 5.5, 3.6, 2.7, 1.9, 1.3, 1.1, 1) added to the composite signal and the solid lines correspond to 100% to 0% noise levels respectively. In the absence of noise, the switching point for all of these cases occurs at the 50% level, which is what is expected. However, in the case where the model configuration levels are consecutive, when the noise level is increased this switching point moves towards higher values, in favor of the model with fewer parameters. The worst case is seen in Level 5 versus Level 6 when the noise level is 100%. However, even in this case even up to 52% noise level, the cutoff threshold is still around 50%

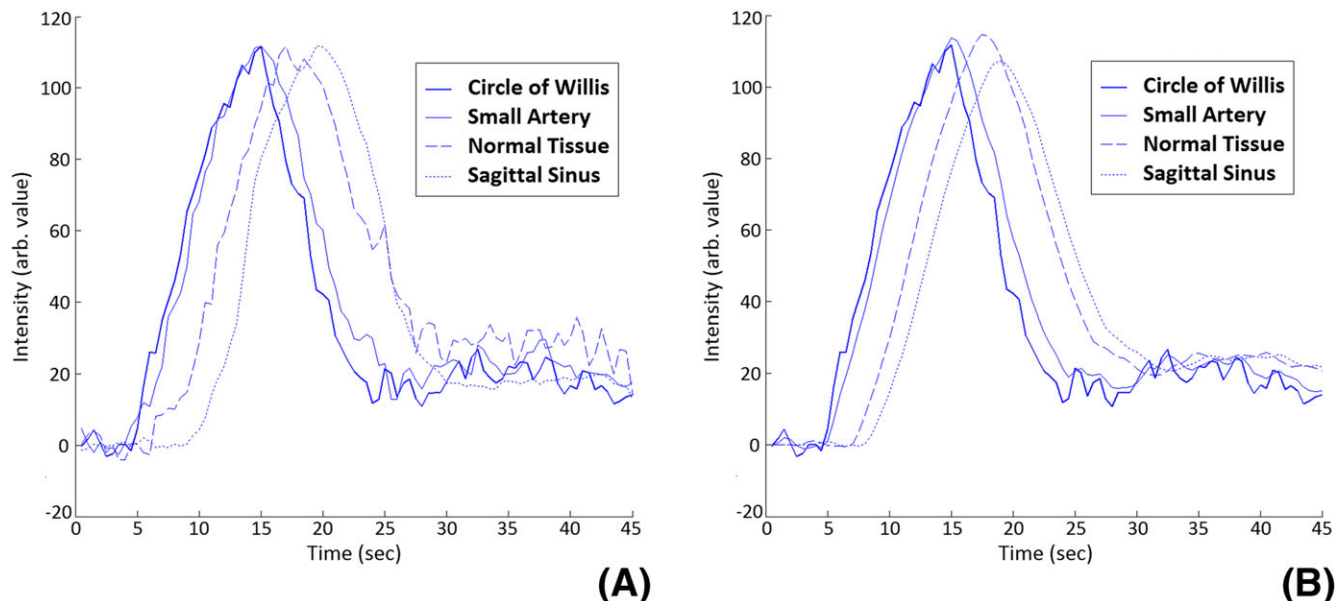


FIGURE 6 A, CA concentration signals sampled from four regions of a DCE-CT image of the human brain. These regions are the circle of Willis, a small artery which is a sub-branch of the MCA, a region in the normal tissue, and the superior sagittal sinus. These signals are scaled to show the relative dispersion and delay of the CA profiles more clearly. B, The reconstructed CA concentration signals corresponding to the signals in A that were created using our proposed fitting and model selection method. As seen here, unlike the results for the other vessels, since our model was not designed for veins and venules, the reconstructed CA concentration signal representing the sagittal sinus does not match the signal sampled from this region

the tissue with healthy vessels. Figure 7A shows the six Akaike weight maps for two slices of a DCE-CT image volume. As seen in this figure, in the Akaike map of the first model configuration, the voxels that represent the major artery from which the AIF has been sampled have the highest Akaike weight, (which have a value very close to unity). As the model configuration index increases, the voxels with the highest value shift from the major arteries to other cerebral regions. In the map corresponding to model configurations 5 and 6, the voxels showing the major veins such as the sagittal sinus have the highest likelihood of belonging to this model configuration. The reason for this is that the transfer function was not designed to describe the changes of the CA concentration profile in the veins and venules, and since in the model fitting step these configurations give the lowest fitting residue, they are selected at the best fitting model configurations.

These probability maps were used to create the blood flow delay maps of the brain seen in Figure 7C,E. Point **R** in this figure shows the reference point where the global AIF was sampled (same profile as the AIF in Figure 2). This AIF was used to estimate the transfer function between **R** and all the voxels in the image. As seen here, the estimated delay time is different at different parts of the brain: the arteries such as the main arteries marked as **A** have a short delay time and other areas of the brain have longer delay times and have values up to 4 s, which is a good approximation of the MTT of the blood flow in the brain.³⁷ As explained above, the profile in veins (such the superior sagittal sinus marked as **B**) cannot be explained using this model, and the estimated delay times in these regions are not valid. As seen in Figure 7E, the tumor (**T**) shows a longer delay time. This long delay time in the tumor area is an overestimation of the actual value. One reason for this may be the extravasation of the CA to the extracellular-extravascular space, which results in changes of the CA concentration profile in this area such that it cannot be explained solely by dispersion and delay. This issue will be addressed in an accompanying paper.³⁸

4 | DISCUSSION AND CONCLUSION

In this study, the first system investigation was performed on a novel vascular model that we have developed to study the changes of the AIF at different levels of the vascular structure, using a transfer function of a single vessel. Our investigation is based on a combination of simplex (for fitting) and AIC (for model selection) methods, and we carried out a simulation study to test our methods and also studied the application of our method in DCE-CT images of the human brain. Our model can analytically explain dispersion of the CA profile at different levels of the vascular tree in the brain without any assumptions about the profile of the CA, using system analysis methods. The simulation results showed high accuracy in finding the level of the CA profile in the vascular tree and the contribution of CA profiles at different levels of the vascular tree. Applying this model to DCE-CT images of the human brain showed that the arrival time of the CA at each voxel matched the expected data.

Our novel semi-empirical model of the brain vascular system is based on laws of fluid dynamics and morphology of the vascular structure in the brain. Our approach is similar to the framework proposed by Gall et al.¹⁸ and Kellner et al.¹⁹ One advantage of this model is that it does not make any assumptions about the profile of the CA (such as it being a gamma variate or Gaussian function, etc.). The vascular model in its current form does not include all aspects of the laws of fluid dynamics and vascular physiology such as turbulence at the bifurcation points in the vessels; but considering the data modalities and also the time resolution of our dynamic experiments, it can explain dispersion in the brain vasculature very well. However, this model assumes no leakage of the CA from the vessels into the extravascular space; leakage can change the profile of the measured tissue response signal. To address leakage, permeability and diffusion parameters should be incorporated into the model. As an extension of our model,

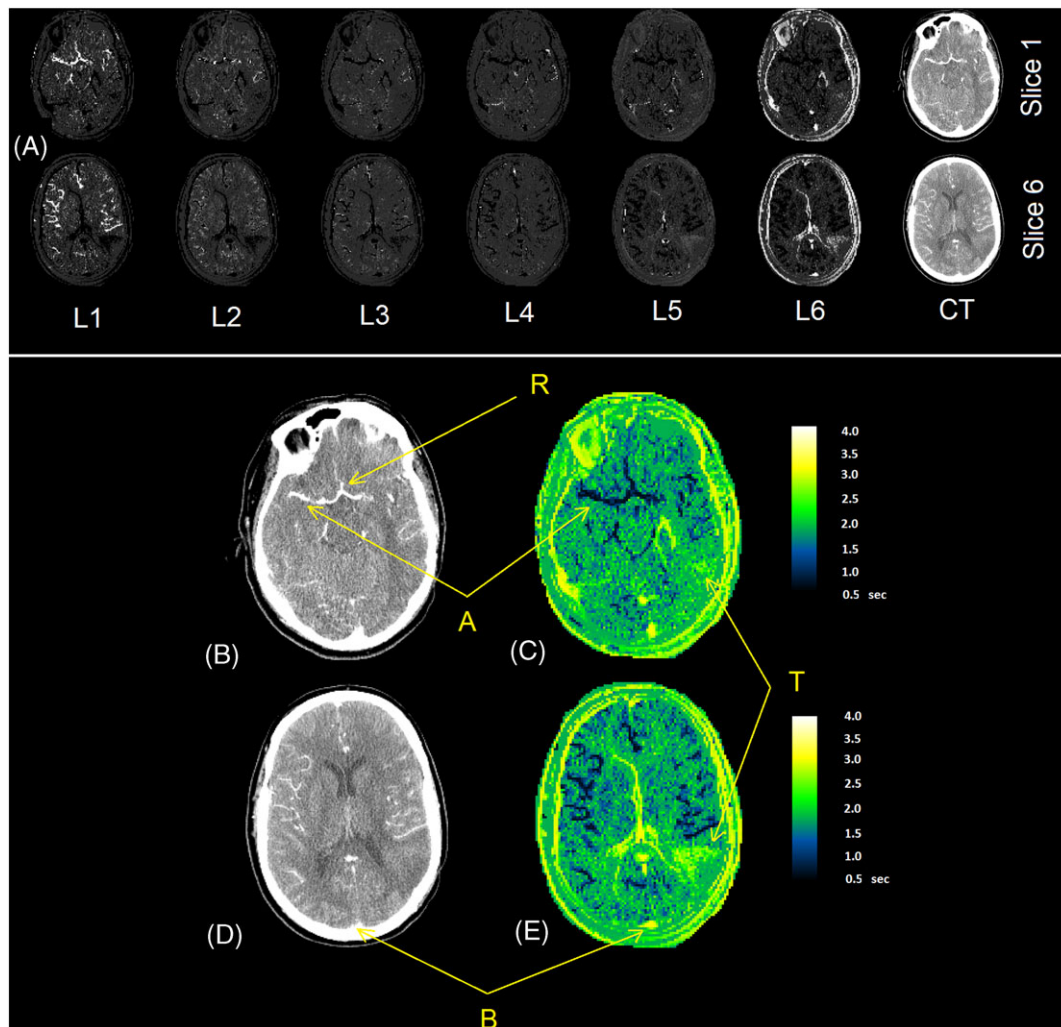


FIGURE 7 A, Akaike weight maps of two slices of the CT image based on the six levels (configurations) of the vascular tree model. The intensity of each voxel in images L1 through L6 shows the likelihood of this voxel belonging to this level in the vascular tree. Based on the Akaike method, the sum of the intensities of every voxel across the six images is unity. The images in the right-hand column are the CT images of the same slice, a few seconds after injection of the CA. As seen in these CT images, all the major vessels have been enhanced in intensity but there is no distinction between the arteries and veins since they are all enhanced. B-E, Enlarged images of the two sections of post injection CT images in A (B,D) and the delay maps (in seconds) created using our method (C,E). 'R' is the reference point for measuring the global AIF. 'A' is the location of one of the main arteries and 'B' shows the superior sagittal sinus. 'T' shows the location of the tumor

we have included and studied the effects of some of these parameters in our model. These will be reported in a separate paper.³⁸ The number of parameters that are directly estimated using the vascular model is two; these are basically the delays of the vascular segments and a scaling factor. However, other parameters can be indirectly estimated using the estimated transfer function.

Our vascular model has demonstrated its application for studying the changes of the AIF at different levels of the vascular structure and for improving the measurement of arrival time of the CA in the dynamic contrast enhanced perfusion measurements. Kellner et al.¹⁹ have described two approaches for measuring the tracer in the vessel segment with laminar flow: the snapshot method, where the CA volume is measured instantaneously, and the flow-type method, where local velocity contribution to the labeled CA volume is considered. Although the flow-type model provides a better theoretical approach, fitting the flow-type model and snapshot model to the ASL data showed that the transfer function of the snapshot model gave better fits to the data than the flow-type

model. On the other hand, the expected bolus dispersions using these two models differ only slightly after passing through a few bifurcations.¹⁹

The interesting point about the vascular transfer function is that it can describe dispersion in a single vessel with only one parameter. Our model mainly describes arteries, arterioles and capillaries, and in order to describe the veins, venules and capillaries more parameters should be added to the model to address the dispersion of the CA profile in the veins more accurately. However, considering the fact that the total volume fraction of capillaries, veins and venules makes up only about 3% of the total brain volume,³⁹ the likelihood of selecting a voxel representing a vein is low. For this reason and also to avoid unnecessary increase of the complexity of our model at this point, we did not include this in our analysis. Despite this, since the transfer function of the veins and venules is the closest to that of the highest level of arterioles in our model, these vessels show the best fit to the transfer functions describing these vessels; the results as seen in the final Akaike weight maps (Figure 7A) show the major veins (such as the

inferior and superior sagittal sinus) having the highest likelihood at the highest model level, which confirms this point.

The good performance of the model fitting and selection method in the simulation studies in presence of noise shows its robustness for finding the vascular branching level of signals for non-simulated data. In the second part of this paper,³⁸ this model will be translated to DCE-MR experiments for estimating permeability parameters in these images. To extend this model to be used for perfusion studies, the tissue input function should be estimated and for this reason the effect of capillaries should be added to the model.

One application of this model and methods introduced in this paper is tissue characterization; based on the vascularity of the tissue, the CA profile can change and this can be used to classify it. As was noted, modeling abnormal vasculature in the brain such as those in tumors can add to the options for possible equations of the transfer function, and by using the same procedure as described in this study different types of tissue can be characterized in the DCE images based on the parameters of the model, which will be part of future work.

In conclusion, we have developed a model of the vascular system of the brain that explains dispersion of the CA profile in different locations in the brain vascular system, and has been tested using DCE-CT and simulated data. Even though at this point only healthy arteries and arterioles have been included in our model, in its current form it can give a good estimate of the transfer functions of most vessels in the brain. Further steps in this research will involve adding parameters to the model to describe certain effects of capillaries and also vascular pathologies that could be used for more accurate estimation of perfusion and permeability characteristics of vessels in DCE images.

ACKNOWLEDGEMENTS

Research reported in this manuscript was supported by the National Institutes of Health under award number RO1NS64134.

CONFLICT OF INTEREST

The authors declare that they have no conflicts of interest in the research.

REFERENCES

- Chan AA, Nelson SJ. Simplified gamma-variate fitting of perfusion curves. In: *2th IEEE international symposium on biomedical imaging (ISBI)*, Arlington, VA, USA. 2004;1067–1070.
- Nestorov I. Whole-body physiologically based pharmacokinetic models. *Exp Opin Drug Metab Toxicol*. 2007;3(2):235–249.
- Sherwin SJ, Franke V, Peiró J, Parker KH. One-dimensional modelling of a vascular network in space-time variables. *J Eng Math*. 2003;47:217–250.
- Blanco PJ, Pivello MR, Urquiza SA, Feijoo RA. On the potentialities of 3D-1D coupled models in hemodynamics simulations. *J Biomechanics*. 2009;42(7):919–930.
- Bagher-Ebadian H, Jafari-Khouzani K, Soltanian-Zadeh H, Ewing JR. A blood circulatory model to estimate the arterial input function in MR brain perfusion studies. *Proc Int Soc Magn Reson Med*. 2008;16:3260.
- Noorizadeh A, Bagher-Ebadian H, Faghihi R, Narang J, Jain R, Ewing JR. Input function detection in MR brain perfusion using a blood circulatory model based algorithm. *Proc Int Soc Magn Reson Med*. 2010;18:5102.
- Calamante F, Morup M, Hansen LK. Defining a local arterial input function for perfusion MRI using independent component analysis. *Magn Reson Med*. 2004 Oct;52(4):789–797.
- Mouridsen K, Friston K, Hjort N, Gyldensted L, Ostergaard L, Kiebel S. Bayesian estimation of cerebral perfusion using a physiological model of microvasculature. *Neuroimage*. 2006;33(2):570–579.
- Calamante F, Gadian DG, Connelly A. Quantification of bolus-tracking MRI: improved characterization of the tissue residue function using Tikhonov regularization. *Magn Reson Med*. 2003;50(6):1237–1247.
- Calamante F, Gadian DG, Connelly A. Delay and dispersion effects in dynamic susceptibility contrast MRI: simulations using singular value decomposition. *Magn Reson Med*. 2000;44(3):466–473.
- Cebral JR, Yim PJ, Lohner R, Soto O, Choyke PL. Blood flow modeling in carotid arteries with computational fluid dynamics and MR imaging. *Acad Radiol*. 2002;9(11):1286–1299.
- Hrabe J, Lewis DP. Two analytical solutions for a model of pulsed arterial spin labeling with randomized blood arrival times. *J Magn Reson*. 2004;167(1):49–55.
- Ozyurt O, Dincer A, Ozturk C. A modified version of Hrabe-Lewis model to account dispersion of labeled bolus in arterial spin labeling. *Proc Int Soc Magn Reson Med*. 2010;18:4065.
- Hernandez-Garcia L, Lee GR, Vazquez AL, Yip CY, Noll DC. Quantification of perfusion fMRI using a numerical model of arterial spin labeling that accounts for dynamic transit time effects. *Magn Reson Med*. 2005;54(4):955–964.
- Kazan SM, Chappell MA, Payne SJ. Modeling the effects of flow dispersion in arterial spin labeling. *IEEE Trans Biomed Eng*. 2009;56(6):1635–1643.
- Gallichan D, Jezzard P. Modeling the effects of dispersion and pulsatility of blood flow in pulsed arterial spin labeling. *Magn Reson Med*. 2008;60(1):53–63.
- Chappell MA, Woolrich MW, Kazan S, Jezzard P, Payne SJ, MacIntosh BJ. Modeling dispersion in arterial spin labeling: validation using dynamic angiographic measurements. *Magn Reson Med*. 2013;69(2):563–570.
- Gall P, Guether M, Kiselev V. Model of blood transport couples delay and dispersion and predicts ASL bolus measurements. *Proc Int Soc Magn Reson Med*. 2010;18:1736.
- Kellner E, Gall P, Gunther M, et al. Blood tracer kinetics in the arterial tree. *PLoS One*. 2014;9(10): e109230.
- Lee SE, Lee SW, Fischer PF, Bassiouny HS, Loth F. Direct numerical simulation of transitional flow in a stenosed carotid bifurcation. *J Biomechanics*. 2008;41(11):2551–2561.
- Truskey GA, Yuan F, Katz DF. *Transport Phenomena in Biological Systems*. 2nd ed. Pearson Prentice Hall: Upper Saddle River, NJ; 2009.
- Gall P, Petersen ET, Golay X, Kiselev V. Delay and dispersion in DSC perfusion derived from a vascular tree model predicts ASL measurements. *Proc Int Soc Magn Reson Med*. 2008;16:627.
- Murray CD. The physiological principle of minimum work: I. The vascular system and the cost of blood volume. *Proc Natl Acad Sci U S A*. 1926;12(3):207–214.
- Sherman TF. On connecting large vessels to small. The meaning of Murray's law. *J Gen Physiol*. 1981;78(4):431–453.
- Turner R. How much cortex can a vein drain? Downstream dilution of activation-related cerebral blood oxygenation changes. *Neuroimage*. 2002;16(4):1062–1067.
- Ferrara LA, Mancini M, Iannuzzi R, et al. Carotid diameter and blood flow velocities in cerebral circulation in hypertensive patients. *Stroke*. 1995;26(3):418–421.
- Uflacker R. *Atlas of Vascular Anatomy: an Angiographic Approach*. 2nd ed. Philadelphia, PA: Lippincott Williams & Wilkins; 2007.
- Wright SN, Kochunov P, Mut F, et al. Digital reconstruction and morphometric analysis of human brain arterial vasculature from magnetic resonance angiography. *Neuroimage*. 2013;82C:170–181.

29. Esposito A. A simplified method for analyzing circuits by analogy. *Mach Des.* 1969;173–177.
30. Lagarias JC, Reeds JA, Wright MH, Wright PE. Convergence properties of the Nelder–Mead simplex method in low dimensions. *SIAM J Optim.* 1998;9(1):36.
31. Posada D, Buckley TR. Model selection and model averaging in phylogenetics: advantages of Akaike information criterion and Bayesian approaches over likelihood ratio tests. *Syst Biol.* 2004;53(5):793–808.
32. Burnham KP, Anderson DR. *Model Selection and Inference: a Practical Information-Theoretic Approach.* New York: Springer; 1998.
33. Brix G, Zwick S, Kiessling F, Griebel J. Pharmacokinetic analysis of tissue microcirculation using nested models: multimodel inference and parameter identifiability. *Med Phys.* 2009;36(7):2923–2933.
34. Ogura A, Miyai A, Maeda F, Hongoh T, Kikumoto R. Comparison of contrast resolution between dynamic MRI and dynamic CT in liver scanning. *Nihon Hoshasen Gijutsu Gakkai zasshi.* 2002;58(2):286–291.
35. Kudo K, Terae S, Katoh C, et al. Quantitative cerebral blood flow measurement with dynamic perfusion CT using the vascular-pixel elimination method: comparison with $H_2^{15}O$ positron emission tomography. *Am J Neuroradiol.* 2003;24(3):419–426.
36. O'Connor JP, Tofts PS, Miles KA, Parkes LM, Thompson G, Jackson A. Dynamic contrast-enhanced imaging techniques: CT and MRI. *Br J Radiol.* 2011;84(2):S112–S120.
37. Ibaraki M, Ito H, Shimosegawa E, et al. Cerebral vascular mean transit time in healthy humans: a comparative study with PET and dynamic susceptibility contrast-enhanced MRI. *J Cereb Blood Flow Metab.* 2007;27(2):404–413.
38. Nejad-Davarani SP, Bagher-Ebadian H, Ewing JR, et al. An extended vascular model for less biased estimation of permeability parameters in DCE-T1 images. *NMR in Biomedicine.* 2017;e3698. <https://doi.org/10.1002/nbm.3698>.
39. Ito H, Kanno I, Iida H, et al. Arterial fraction of cerebral blood volume in humans measured by positron emission tomography. *Ann Nucl Med.* 2001;15(2):111–116.

How to cite this article: Nejad-Davarani SP, Bagher-Ebadian H, Ewing JR, et al. A parametric model of the brain vascular system for estimation of the arterial input function (AIF) at the tissue level. *NMR in Biomedicine.* 2017;30:e3695. <https://doi.org/10.1002/nbm.3695>

APPENDIX

DERIVATION OF THE TRANSFER FUNCTION OF A SINGLE VESSEL WITH LAMINAR LAW

To derive an equation for the transfer function of a vessel, we start by finding the volume of the CA and the total volume of the fluid exiting a vessel with the length of D_0 , as a function of time. Initially CA is introduced into the entrance of the vessel in the form of a step function, and after flowing through the vessel it forms a parabola. The equation of the surface of the parabola is written as

$$z = v_0 \left(1 - \frac{r^2}{R^2} \right) t \quad (\text{A.1})$$

where R is the radius of the vessel, r the radial distance of the parabola surface from the axis of the vessel and z the distance from the opening of the vessel. After time $t_0 = D_0/v_0$ the tip of the parabola reaches the end of the vessel, and at time $t = D/v_0$ it reaches the plane $z = D$ (assuming that the fluid continues to flow in a cylindrical form). The volume of the CA enclosed between the between the planes D_0 and D can be calculated as

$$V_{CA} = \frac{\pi}{2} R^2 v_0 t \left(1 - \frac{D_0}{v_0 t} \right)^2 \quad (\text{A.2})$$

Prior to time $t = t_0$ there is no CA exiting the vessel so the average CA concentration is zero during this time. The total volume of fluid exiting the vessel between the times t_0 and t can be calculated as

$$V_{tot} = \frac{\pi}{2} R^2 v_0 t \left(1 - \frac{D_0}{v_0 t} \right) \quad (\text{A.3})$$

To find the CA concentration of the fluid exiting the vessel the volume of the CA exiting the vessel in an infinitesimal time should be divided by the total volume of fluid exiting the vessel in the same time,

$$CA_c = \frac{dV_{CA}/dt}{dV_{tot}/dt} = 1 - \left(\frac{t}{t_0} \right)^2 \quad \text{for } t > t_0 \quad (\text{A.4})$$

and since this is the response to the unit step function, the transfer function equation can be found by differentiating this with respect to time:

$$h(t) = \begin{cases} 0 & t < t_0 \\ \frac{2t_0^2}{t^3} & t \geq t_0 \end{cases} \quad (\text{A.5})$$